

Programmable Switching of Molecular Transitions via Plasmonic Toroidal Nanoantennae

Arda Gulucu^{1,2} and Emre Ozan Polat^{1,2,*}

¹*Department of Physics, Bilkent University, 06800, Ankara, Turkey*

²*UNAM – National Nanotechnology Research Center and Institute of Materials Science and Nanotechnology, Bilkent University, 06800, Ankara, Turkey*

**Corresponding author: emre.polat@bilkent.edu.tr*

Abstract

The ability to switch and program molecular transitions via deterministically located plasmonic nanoantennae presents opportunities for wide spectrum of applications from biosensors to quantum computing. Due to its topology, toroidal nanoantenna (TNA) focuses immense amount of three-dimensional (3D) local electric field by toroidal moment while allowing pre and post positioning around quantum emitters (QEs). Here, we report complete switching of molecular transition energies of quantum objects (QOs) with modulation depth of 99.9% over 2840-fold radiative enhancement. At optimized TNA geometries, Fano interference between the broadband plasmonic continuum and narrow quantum transitions of QOs suppresses both radiative and non-radiative decay channels near 850 nm, yielding an observable full switching that traps energy within the hybrid mode instead of re-emitting it. To show the promises of the concept, we further demonstrate systems with multiple QOs where spectral degeneracy enhances the transparency bandwidth, while detuning generates distinct minima, enabling individually addressable spectral responses. These results establish plasmonic TNA as a promising architecture for spectral detection of single or multi-molecule configurations with high sensitivity and empowers the user for the implementation of quantum mode switches to be used in photonic processing.

Introduction

Plasmonics exploits the collective oscillations of free electrons at metal-dielectric interfaces to concentrate electromagnetic energy into nanoscale volumes known as “hotspots” [1,2]. Localized surface plasmon resonances (LSPRs) in metallic nanoparticles generate intense electric fields near their surfaces, enabling surface-enhanced Raman scattering, fluorescence modulation, and nanoscale sensing [3–6]. Spherical and rod-shaped nanoparticles have been extensively studied in the context of field localization [7–9]. Unlike commonly used spheres, rods or rings, TNA supports closed poloidal displacement currents that realize a toroidal (anapole) moment, squeezing fields into the inner rim with small mode volume [10,11]. Offering unique confinement properties, the topology of a metallic TNA produces a 3D hotspot volume with simultaneous radial and axial localization, supported by circulating plasmon modes [12–16]. This configuration provides versatile tunability of resonance wavelength through its aspect ratio while delivering a high local density of optical states (Purcell enhancement [17]) and multipolar mode mixing [18]. These features make toroidal plasmonic resonators a strong contender for engineering strong light–matter interactions at deterministic emitter locations.

When a narrow discrete resonance interacts coherently with a broad plasmonic continuum, their interference gives rise to an asymmetric Fano lineshape, manifested as a sharp dip or

transparency window within the otherwise broad scattering spectrum [19,20]. The discrete state can originate from QOs such as molecules, quantum dots, or excitons possessing intrinsically narrow linewidths [21–26]. These hybrid plasmon-QO Fano resonances produce spectrally sharp and tunable features with enhanced local fields and strong dispersion enabling promising results in high-sensitivity sensing, optical switching, low-threshold lasing, and nonlinear photonic functionalities [27,28].

Here, we present a novel approach to control and switch the discrete quantum modes over the highly enhanced photoluminescent (PL) spectrum of a QE placed in proximity to a TNA. Unlike previous plasmon–exciton Fano studies that could not achieve a complete switching behavior by the demonstration of spectral Fano modulation [29–32], and Fano/metasurface implementations that require complex multi-resonator unit cells or 3D metamaterial architectures [33–37], we demonstrate that a molecule with a Lorentzian dielectric function in resonance with the QE’s emission completely switches off the radiative (and non-radiative decay) that are initially boosted by a factor of 2840 (and 1056) nearby TNA. The fact that the narrow resonance of employed molecule doesn’t need to radiate light; (it only needs to modify the local field through a sharp variation in its complex polarizability $\epsilon(\omega)$) makes our approach general for the implementation of TNAs around various QOs such as defect centers, molecules, quantum dots and any possible QO with intrinsically narrow linewidth.

The strict control of the quantum mode switches is provided through the toroid’s aspect ratio that optimizes the local density of optical states (LDOS) thereby yields spectral enhancement. Interference of a closely located QO induces a Fano transparency in the enhanced spectrum, yielding a complete switching of quantum modes over the plasmonic continuum. Our approach is based on the specific regime of TNA aspect ratios, that provides a large span of emitter-antenna distances where the QE radiative decay rate dominates over non-radiative counterpart. Presented numerical study simulates the hybrid system consisting of QOs, TNAs and QEs through finite-difference time domain (FDTD) simulations and reports a framework of crucial cases for the practical applications. The experimental implementation of the approach is viable through various fabrication methods provided that the toroidal structures can be fabricated around QEs, and the QOs can be imposed later. Alternately, the TNA can be located around a defect center, ensuring deterministic alignment.

To show the promises of our approach, the investigation is extended from single QO to multi-QO configurations demonstrating that spectral degeneracy enhances the transparency bandwidth, while detuning among multiple QO (such as the Stark effect [38]) generates multiple minima that are individually addressable over the plasmonic continuum. The reported results provide a benchmark for spectral sensing and manipulation of quantum states thus, we anticipate that the efficient quantum mode switching would yield applications where the related wavelength needs to be selectively sensed (or blocked) such as super resolution bioimaging [39], quantum sensing [40], programmable photonic circuits [41] and future display technologies [42].

Results

We first consider a system consisting of a dipole QE positioned at a distance d from a silver TNA with major radius R and cross-sectional radius α (**Figure 1a**). **Figure 1b** shows the snapshot of the electric field intensity distribution (at $t \approx 0.14$ ps) sourced from the dipole emission of QE and localized around the TNA. (The video of complete EM interaction can be

found at **Supplementary Video 1**). By varying the aspect ratio α/R , the plasmonic resonance wavelength (λ_{res}) of the TNA can be tuned. We found that, for a constant 60 nm of total TNA radius ($R + \alpha = 60$ nm), increasing the aspect ratio from 0.1 to 1 shifts the λ_{res} (**Figure 1c**) from NIR to UV-Vis yielding a broad spectrum nanoantenna to be implemented for variety of QEs. In compliance with the analytical solutions, as the aspect ratio (and hence the effective volume) of the toroid gets smaller, resonance wavelength red shifts [12]. Similarly, as the ratio approaches to unity, the dipole experiences the TNA as a metal nanosphere of radius $R + \alpha$, thus λ_{res} becomes constant for the values above 0.7 (**Figure 1c**).

Figure 1d shows the normalized radiative and non-radiative decay rates for the emitter-antenna distance of $d = 3$ nm and total TNA radius of $R + \alpha = 60$ nm. While one may expect non-radiative decay to dominate at short antenna distance due to Förster-type energy transfer, we find a counterintuitive window in which the radiative decay exceeds the non-radiative loss. Specifically, peaking around $\alpha/R = 0.2$, the radiative channel is enhanced between $\alpha/R = 0.2$ and 0.6 as highlighted in the inset of **Figure 1d**. The corresponding λ_{res} and normalized decay rates for different aspect ratios are tabulated in **Table 1**.

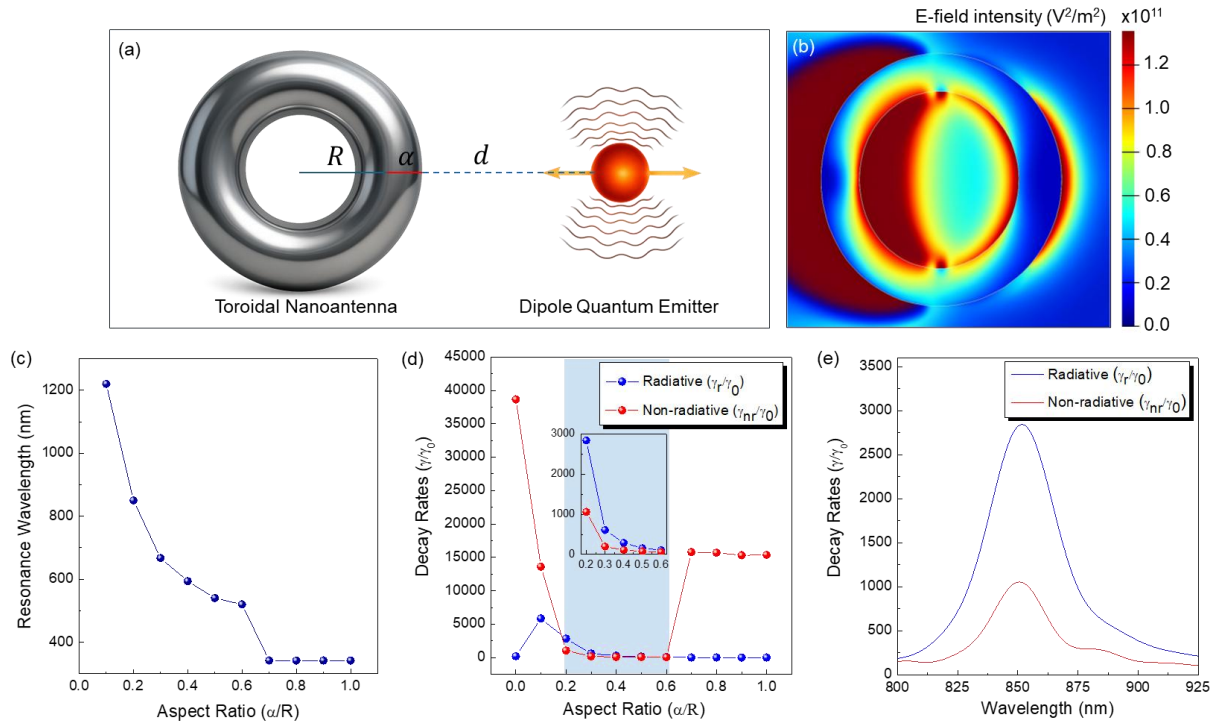


Figure 1. (a) Schematic illustration of the quantum emitter-toroidal nanoantenna (QE-TNA) system for plasmonic enhancement. A dipole QE (red) located at distance d away from a silver TNA, with a major radius R and cross-section radius α . (b) Snapshot of local electric field intensity ($|E_{loc}|^2$) at $t \approx 0.14$ ps for the presented QE-TNA system. Color bar shows the E-field intensity scale. (c) Resonance wavelengths for increasing aspect ratios (α/R). By changing the ratio between 0.2 and 1, one can yield a broadband range of resonance wavelengths from NIR to UV-Vis (d) Normalized decay rate (γ/γ_0) values at resonance wavelength (850 nm) with respect to TNA aspect ratio (for $d = 3$ nm). Inset shows the intermediate aspect ratio regime where the radiative decay rates (γ_r/γ_0) overcome the non-radiative (γ_{nr}/γ_0) counterparts. (e) Decay rate spectra of QE-TNA coupling. For the optimal condition of $\alpha/R = 0.2$ the

enhancement of LDOS boosts the radiative decay rate over the non-radiative counterpart around the resonance wavelength of $\lambda_{res} = 850$ nm.

This intermediate regime can be understood analytically via the Purcell factor,

$$F_p = \frac{\gamma_{tot}}{\gamma_0} = \frac{3}{4\pi^2} \left(\frac{\lambda}{n}\right)^3 \frac{Q}{V_{eff}}$$

where $\gamma_{tot} = \gamma_r + \gamma_{nr}$ is the total decay rate of the emitter in the presence of a nanoantenna, γ_0 is the free space decay of the emitter, λ is the wavelength, n is the refractive index of the environment, Q is the quality factor and V_{eff} is the effective mode volume. The reduction in aspect ratio both redshifts the resonance (larger λ) and compresses the effective mode volume (smaller V_{eff}). These effects jointly increase the LDOS and hence the Purcell factor F_p , with the modest reduction in Q being outweighed. Within the optimal range ($\alpha/R = 0.2$ - 0.6), LDOS enhancement couples predominantly to radiative channels, effectively rendering the plasmonic TNA as a cavity despite its modest Q . For smaller aspect ratios ($\alpha/R < 0.2$), the dipole enters a Rayleigh absorption regime dominated by loss, while for larger ratios ($\alpha/R > 0.6$) the structure behaves increasingly like a silver nanosphere, where Ohmic dissipation prevails.

Table 1: Complete parameter set of demonstrated dipole QE-TNA coupling.

Aspect Ratio (α/R)	Plasmon Resonance Wavelength λ_{res} (nm)	Normalized Radiative Decay Rate $\gamma_r/\gamma_0 (\times 10^3)$	Normalized Non- radiative Decay Rate $\gamma_{nr}/\gamma_0 (\times 10^3)$
0.1	1220	5.870	13.60
0.2	850	2.840	1.056
0.3	667	0.608	0.195
0.4	600	0.284	0.109
0.5	542	0.155	0.073
0.6	514	0.104	0.056
0.7	412	0.020	15.80
0.8	412	0.015	15.70
0.9	412	0.017	15.33
1.0	412	0.013	15.38

We therefore identify $\alpha/R = 0.2$ as the optimal geometry for radiative efficiency, enabling strong enhancement of emission rates ($\gamma_r/\gamma_0 = 2840$) that is not suppressed by the non-radiative losses ($\gamma_{nr}/\gamma_0 = 1056$) around $\lambda_{res} = 850$ nm (**Figure 1e**). Although a single quantum emitter typically exhibits a narrow Lorentzian emission profile, the broadband response between 800 nm and 900 nm shown in **Figure 1e** represents the Purcell enhancement spectrum of the plasmonic environment rather than the intrinsic linewidth of the emitter. The

TNA supports a broad plasmonic continuum that modifies the LDOS experienced by the emitter. Consequently, the radiative and non-radiative decay rates inherit this broadband character, reflecting the spectral density of plasmonic modes rather than the emitter's transition linewidth. This optimized geometry and the aspect ratio regime that provides observable emission enhancement will form the foundation for Fano interference switching of single- and multi-emitter systems, as will be discussed in the followings.

Next, a single molecule with a sharp Lorentz dielectric function is placed at the center of TNA (**Figure 2a**). When coupled to the broadband plasmonic continuum of the QE-TNA system, this phase-modulated polarization interferes with the plasmonic field, forming a hybrid system that supports a Fano-type interference between narrow and broad optical channels. The interference modifies the overall scattering cross-section, producing an asymmetric Fano line shape. **Figure 2b and c** show the normalized radiative (γ_r/γ_0) and non-radiative (γ_{nr}/γ_0) decay rate spectra. For the bare QE-TNA system, both γ_r and γ_{nr} vary smoothly, reflecting conventional broadband plasmonic dissipation. When a QO of 20 nm radius is introduced, a sharp suppression appears around $\lambda = 850$ nm, marking the Fano transparency. The complementary reduction in both decay channels indicates that destructive interference at this wavelength traps energy within the hybrid mode instead of re-emitting it. Although both decay channels can be modulated efficiently, it is worth noting that the complete switching (from $2840\gamma_0$ to 0) behavior of radiative decay channel is not identical to the non-radiative decay channel due to the fundamental losses via electron-phonon and phonon-phonon interactions yielding a modulation from $1056\gamma_0$ to $249\gamma_0$. **Figure 2d** depicts the near-field intensity maps for resonance and off-resonance wavelengths around the transparency window. While strong localized fields are observed for off-resonance wavelengths around the TNA surface, At $\lambda = 850$ nm the field intensity completely collapses due to the destructive interference between the QO-induced polarization and the plasmonic continuum, demonstrating the optical switching behavior of the Fano resonance. The suppression of LDOS within the Fano transparency window can be clearly seen. The overall Purcell enhancement is given in **Figure 2e** that compares the Purcell factor spectra for the two configurations: (i) the bare plasmonic continuum of the QE-TNA system (orange curve), and (ii) the hybrid QE-TNA-QO system (cyan curve). The introduction of the narrow QO resonance converts the smooth continuum response into an asymmetric profile with a pronounced transparency dip. This minimum corresponds to the destructive interference point, where the real part of the QO self-energy shifts the resonance frequency slightly (from 348 THz \sim 353 THz), consistent with the hallmark of Fano interference between discrete and continuum states [43]. The efficient enhancement and suppression of the Purcell factor via demonstrated system bypasses the need for complex cavity constraints thereby allowing for multipixel arrangement in 3D that can be individually addressable.

To provide a detailed investigation of the configuration and present a useful model for experimental implementations, we demonstrate the spatial orientation dependence of the system by scanning the emitter-antenna separation “ d ”. The normalized decay rates are recorded and fitted to an exponential function revealing the resonance dynamics of the hybrid system. **Figure 3a** shows the normalized radiative and non-radiative decay rates at 850 nm with respect to emitter-antenna separation in the absence of central QO. Extracted peak γ_r and γ_{nr} values are curve fitted to an exponential distance function of the form $(y(d) = e^{a+bd+cd^2})$, with constants a, b, c in compliance with the previous works (See **Numerical Methodology** Section) [6,44].

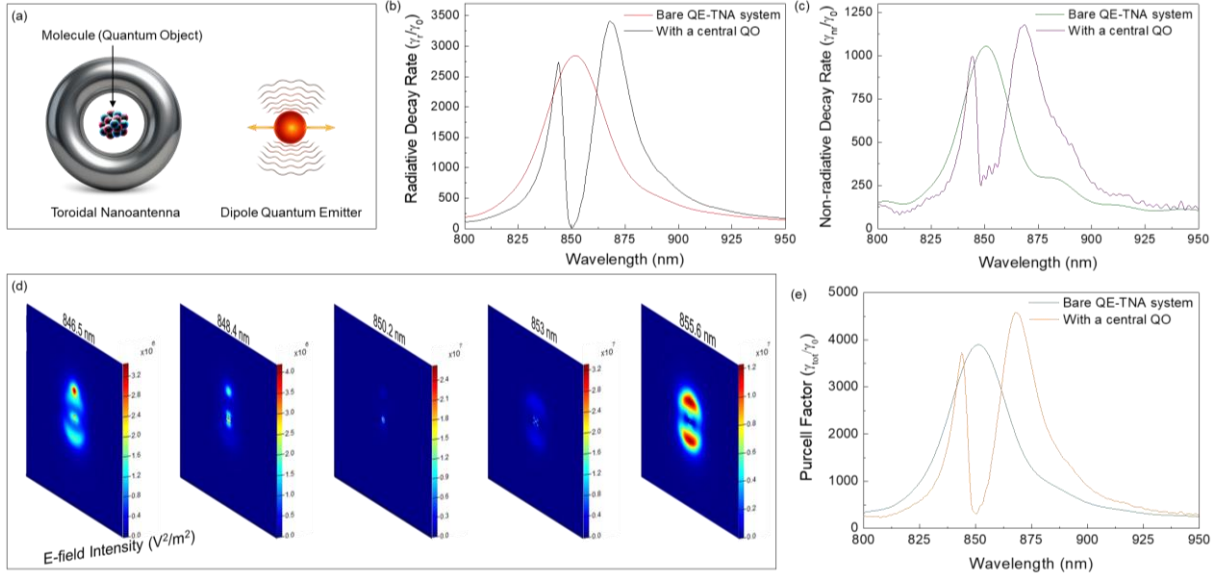


Figure 2. (a) Schematic of the hybrid system depicting the QE-TNA coupling to a central molecule (QO). The dispersive QO introduces a phase-shifted polarization that interferes with the broadband plasmonic continuum of the TNA, producing a Fano-type hybrid mode. (b) Normalized radiative decay rate (γ_r/γ_0) of the system with and without QO. (c) Normalized non-radiative decay rate of the system with and without QO. The introduction of the QO leads to a sharp suppression in both radiative and non-radiative channels around $\lambda = 850$ nm, indicating destructive interference and energy trapping within the hybrid mode. (d) Electric field intensity maps at resonant and off-resonant wavelengths around the transparency region. The collapse of near-field enhancement at the resonance and the enhancement at the off-resonance wavelengths around the transparency window are clearly visible. (e) Purcell factor spectra of the system. The emergence of a narrow transparency dip in the Purcell factor confirms the Fano interference between the discrete QO resonance and the plasmonic continuum.

For large separations $d \gg 50$ nm, both decay rates converge to unity, indicating a transition to free-space behavior. As d decreases, non-radiative decay gradually rises, while radiative decay increases abruptly at very small gaps, an unusual trend for metal based plasmonic systems. Throughout the entire range, the radiative decay rate remains dominant, a result attributed to the toroidal geometry and optimized aspect ratio of the antenna. Therefore the presented configuration effectively bypasses non-radiative Förster resonant energy transfer (FRET) based near-field interactions that typically emerge at sub-10 nm separations and allows the observation of ultimate enhancement factors.

Figure 3b shows the modulation of radiative decay spectra with respect to QE-TNA distance. ($d = 3, 4, 5, 10, 15, 20, 25, 30, 40, 50$ nm). Each spectrum exhibits a characteristic Fano transparency dip near 850 nm with different modulation depths. As the separation increases, the dipole-plasmon coupling weakens, causing the destructive interference responsible for the Fano cancellation to become progressively less pronounced. To put this into context, **Figure 3c** quantifies the percentage intensity of Fano transparency ($\frac{\Delta I}{I}$ %), defined as the relative suppression of the radiative decay rate at the resonance. At $d = 3$ nm, transparency reaches 99.9 % and remains constant up to a distance of $d = 10$ nm, which provides a distance window for the complete switching of quantum modes. After 10 nm transparency modulation experiences

a minimal decrease to 97.8 % at the distance $d = 50$ nm. This intact switching behaviour over large span of distances allows a design freedom for experimental applications.

Our analysis is extended beyond the single QO scenario due to the necessity of multiple molecule configurations in practical applications. The investigated case with the single central molecule revealed the fundamental Fano interference between a QO and the plasmonic continuum of the TNA, opening pathways for practical implementations involving several QOs. Such collective coupling can significantly modify the radiative response, leading to tunable interference effects and new spectral features. To capture this behavior, we introduce additional molecules positioned within the 3D hotspot region of the TNA. In this way, we demonstrate how the inter-molecular spacing and spectral detuning influence the overall spectral switching dynamics.

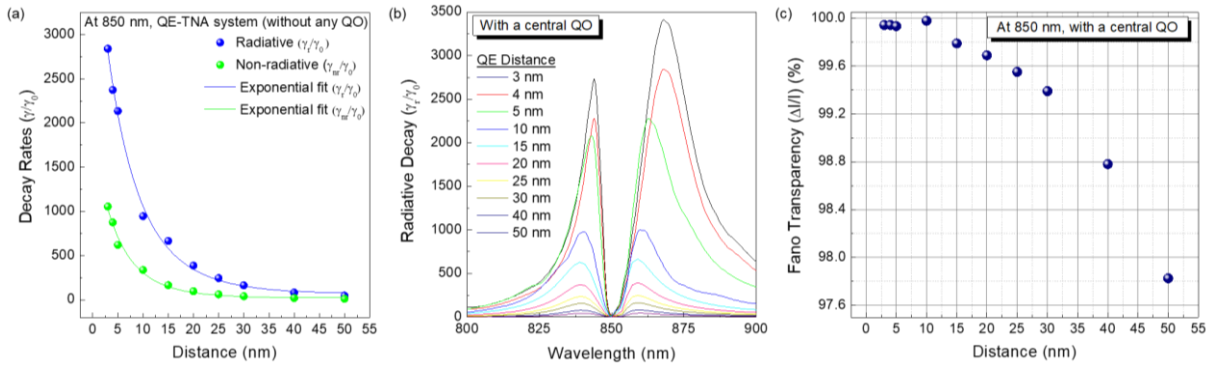


Figure 3. Spatial configuration dependence of the hybrid system. **(a)** Normalized radiative and non-radiative decay rates at QE's emission wavelength (850 nm) in the absence of the central QO. Due to the TNA topology, radiative decay remains superior at all distances ($d = 3-50$ nm) preventing the suppression of the observable enhancement due to non-radiative decay. Exponential curve fitting reveals the free-space transition at large separations **(b)** Radiative decay spectra for the distance regime ($d = 3-50$ nm), exhibiting a characteristic Fano transparency dip around QO's Lorentzian dielectric function in resonance with the QE's emission at 850 nm. With increasing d , dipole-plasmon coupling weakens and the interference contrast diminishes. **(c)** Percentage Fano transparency with respect to dipole QE-TNA distance " d ". While complete switching of quantum modes is possible below 10 nm, the modulation depth shows minimal change from 99.9% to 97.8% in $d = 10-50$ nm regime yielding an intact modulation regime for practical applications.

To extract the decay spectrum and the corresponding Fano switching for a single and multiple QO configurations, we fixed the dipole QE (at $d = 3$ nm) and the central molecule (QO-1 at the center of TNA). Then, 3 external QOs of 20 nm radii are positioned around the TNA respectively with a lateral separation of 5 nm at each direction (**Figure 4a**). When all QOs are in resonance at 850 nm we found that the Fano bandwidth broadens by the addition of individual QOs (**Figure 4b**). While a single molecule provides a transparency bandwidth of 14 nm, the full width at half maximum (FWHM) enlarges to 22 nm, 27 nm and 34 nm respectively for 2, 3, and 4 QOs. Resulting broader Fano dip does not exhibit an important shift in the transparency wavelength, yielding the resonance frequency intact over the spectrum. Due to interference of multiple discrete channels enhancing destructive interference within the plasmonic continuum, we recorded a slightly stronger transparency with increasing number of QOs. However, the effect is minimal since the dipole QE-TNA system was set for optimum performance yielding

maximum available transparency (99.9%) at $d=3$ nm, for $\alpha/R = 0.2$. (See **Figure 3c** and **Table 1**).

Having established the dynamics of multiple resonant QOs (**Figures 4b**), we next examine the effect of spectral detuning between the QOs. In realistic systems, perfect spectral resonance among multiple quantum emitters (QOs) is rarely maintained, since local environmental inhomogeneities, applied electric fields, or mechanical strain can shift their transition energies. For instance, the quantum-confined Stark effect (QCSE) is widely used to tune the emission or absorption wavelength of quantum dots or single molecules by applying static electric fields [45]. Controlled detuning can also be introduced intentionally via such external fields or via strain engineering, as demonstrated in strain-tunable quantum dots and layered material emitters [46]. **Figure 4c** shows the radiative decay spectra of double QOs (QO-1 and QO-2 only) when various frequency tuning rates are present within. For simplicity, we kept the QO-1 in the same resonance wavelength (850 nm) while applying various tuning rates to the QO-2. Interestingly, the detuning of the individual QOs shows a pronounced effect in the plasmonic continuum, shifting the second transparency dip to larger wavelengths with increasing detuning rate (**Figure 4c**). For the tuning rates of 26.4 and 32.8 and 48.6 meV we found that the second transparency window for QO-2 emerges at 865, 870 and 880 nm with bandwidths of ~ 10 nm.

To show the promises of our approach we demonstrate multiple QOs around the 3D hotspot region of TNA for practical applications requiring the sensing (or bypassing) the spectral signals from specific molecules. **Figure 4d** shows the fingerprints of four QOs as a transparency dip within the radiative decay spectra of the hybrid system. When detuned QOs are placed at a fixed distance, we observed that each detuned QO produces its own Fano dip at the corresponding resonance demonstrating that multiple spectral minima can coexist within the same plasmonic continuum. The distinct transparency dips are observed at 850, 865, 870, 880 nm for the detuning rates of 0, 26.4, 32.8 and 48.6 meV, respectively. This demonstrates the switching (or sensing) behaviour for individual molecules within an ensemble. We emphasize that the complete switching of all individual quantum modes are only possible through the maximized local electric field regions around and within TNA and indeterministic placement of molecules may not translate into a meaningful spectral dip in the plasmonic continuum. In addition, the large number of QOs or clustering molecules may suppress the observation of the reported phenomena. These results altogether demonstrate the phenomenon of individually addressable quantum mode switching over plasmonic continuum with efficient modulation depths when deterministic positioning is viable through the TNA topology.

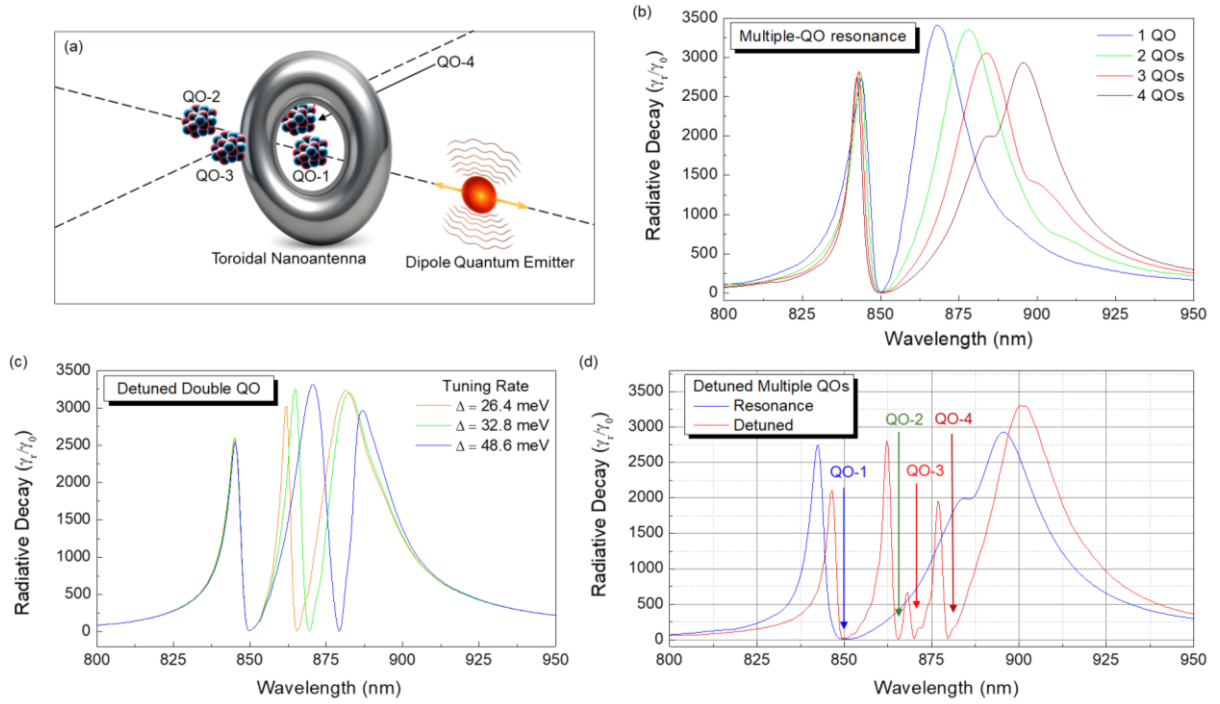


Figure 4. Individually addressable switching and sensing of multiple molecules **(a)** Schematic of the hybrid system consisting of four QOs coupled to an Ag TNA driven by a dipole QE. While the central molecule (QO-1) is fixed within the TNA, external QOs are brought one by one into the 3D hotspot region of TNA. **(b)** Radiative decay spectra for multiple QOs in resonance that are coupled to TNA at a fixed 5 nm separation at each direction. The inclusion of individual QOs enhances the dip asymmetry while broadening it. **(c)** Radiative decay spectra for the detuned double-QO configuration (QO-1 and QO-2 only). Slight differences in transition energies of molecules yields corresponding transparency dip in the plasmonic continuum. **(d)** Radiative decay spectra for the detuned multiple QOs. Fano dips at respective zero-phonon-line wavelengths, leading to individually addressable multiple-dip behavior when four detuned QOs are included.

Conclusion, Discussion and Outlook

In this work, we numerically demonstrated a TNA that emulates a photonic cavity within a specific range of aspect ratios. We developed a comprehensive numerical framework to engineer Fano-resonance phenomena in a hybrid platform composed of a silver plasmonic TNA, a point dipole QE, and one or more narrow Lorentzian-dielectric QOs representing molecules. Treating each QO as a discrete narrow-band oscillator evanescently coupled to the TNA, we performed extensive FDTD simulations to:

1. Identify a pronounced Fano transparency dip at $\lambda \approx 850$ nm due to TNA topology, originating from interference between the broadband TNA plasmon continuum and the narrow QO resonance. The efficiency of the modulation depth (over $2840\gamma_0$) yields complete switching and high sensitivity for practical applications.
2. Demonstrate that the Fano-dip transparency reaches a complete transparency (99.9%) for optimal emitter–antenna separations, and TNA provides a large span of distances ($d = 3\text{-}50$ nm) for design freedom in experimental implementations.

3. Introduce multiple QOs within the 3D hotspot region of TNA that broadens the Fano dip when QOs are spectrally resonant and leads to distinct transparency minima when they are spectrally detuned.

Experimental implementation of the presented concept can be realized by coupling a silver TNA to a narrow-line quantum emitter operating in the near-infrared, such as the V1 silicon-vacancy center in 4H-SiC (≈ 861 nm) or a defect center in hBN (550-850 nm band), and probing the predicted Fano-assisted modulation of the emitter's decay rate using a co-localized fluorescent dipole tuned to the same spectral window near 850 nm [47–49]. To that end, we demonstrated an interval that the toroidal geometry remains active for (aspect ratio regime from 0.2 to 0.6), broadband operation with the fabrication of various TNA geometries.

While extending this design into arrays may offer a powerful route toward multifunctional photonic metasurfaces [50], the proposed hybrid system, exhibiting sharp, high-contrast Fano transparency dips in the radiative decay spectrum, is well suited for label-free, real-time biomolecular sensing at the single-molecule level [51]. Moreover, exploiting the presented single and multiple dip concepts within a lithographically compatible toroidal geometry, promises applications in lab-on-chip biosensors with sub-picomolar sensitivity [52]. reconfigurable dual-band filters, slow-light elements for integrated photonics [53,54] and voltage-gated fluorescence switching or dual-colour spacer cavities for quantum-photonic and bio-imaging technologies [55,56]. We further anticipate that suppressing both radiative and non-radiative decay rates traps the energy within the molecule instead of re-emitting, thereby possessing possible solutions for programmable emissions in future photonic technologies.

Methodology

Theory

For a quantitative interpretation, we approximate the TNA by its dominant single bright quasinormal mode (QNM) with annihilation (creation) operator a (a^\dagger) and resonance frequency ω_c . The QNM is leaky, with total linewidth $\kappa = \kappa_{\text{rad}} + \kappa_{\text{nr}}$, where κ_{rad} accounts for radiation to free space and κ_{nr} for ohmic (absorptive) loss in the metal. A two-level emitter with lowering (raising) operator σ (σ^\dagger) and transition frequency ω_e sits at position \mathbf{r}_e with transition dipole $\boldsymbol{\mu} = \mu \hat{\mathbf{e}}$. The radiative bath (free-space continuum) modes are $\{b_k\}$ and the ohmic bath modes are $\{c_q\}$. The use of QNMs and their normalization for open, dissipative nanoresonators follows standard treatments [57,58].

In the weak-drive, linear-response regime (rotating-wave approximation), the system Hamiltonian reads:

$$\begin{aligned} \frac{H}{\hbar} = & \omega_c a^\dagger a + \omega_e \sigma^\dagger \sigma + (ga\sigma^\dagger + h.c.) + \sum_k \omega_k b_k^\dagger b_k + \sum_q \omega_q c_q^\dagger c_q + \sum_k (\eta_k a^\dagger b_k \\ & + h.c.) + \sum_q (\eta_q a^\dagger c_q + h.c.) \end{aligned} \quad (1)$$

The emitter–mode coupling rate is

$$g = \frac{\boldsymbol{\mu} \cdot \mathbf{E}_c(\mathbf{r}_e)}{\hbar} \sqrt{\frac{\hbar \omega_c}{2\epsilon_0}} \frac{1}{\sqrt{U_c}}, U_c \propto V_{\text{eff}}, \Rightarrow g^2 \propto \frac{\mu^2}{V_{\text{eff}}} |\hat{\mathbf{e}} \cdot \mathbf{E}_c(\mathbf{r}_e)|^2, \quad (2)$$

where $\mathbf{E}_c(\mathbf{r})$ is the (properly normalized) QNM field, U_c its normalization energy, and V_{eff} the effective mode volume at \mathbf{r}_e . QNM-based V_{eff} and mode normalization for leaky systems are discussed in detail in Refs [58,59].

The total spontaneous-emission rate of the emitter in an inhomogeneous environment is governed by the electromagnetic Green tensor G_{ij} :

$$\gamma_{\text{tot}}(\omega) = \frac{2\omega^2}{\hbar\epsilon_0 c^2} \mu_i \mu_j \Im G_{ij}(\mathbf{r}_e, \mathbf{r}_e; \omega). \quad (3)$$

Near a single bright QNM, $\Im G$ is Lorentzian,

$$\Im G(\mathbf{r}_e, \mathbf{r}_e; \omega) \simeq \frac{A(\mathbf{r}_e)}{(\omega - \omega_c)^2 + (\kappa/2)^2} \frac{\kappa}{2}, \quad A(\mathbf{r}_e) \propto \frac{|\hat{\mathbf{e}} \cdot \mathbf{E}_c(\mathbf{r}_e)|^2}{V_{\text{eff}}}. \quad (4)$$

On resonance ($\omega = \omega_c$),

$$\gamma_{\text{tot}}^{(\text{res})} \propto \frac{\mu^2}{\hbar^2} \frac{1}{V_{\text{eff}}} \frac{1}{\kappa}. \quad (5)$$

Equivalently, with the Purcell form,

$$F_P \equiv \frac{\gamma_{\text{tot}}}{\gamma_0} = \frac{3}{4\pi^2} \left(\frac{\lambda}{n}\right)^3 \frac{Q}{V_{\text{eff}}}, \quad Q \equiv \frac{\omega_c}{\kappa}, \quad (6)$$

which is the canonical expression in the high- Q (Hermitian) limit, and admits rigorous generalizations to lossy leaky modes via QNMs.

Because the mode energy leaks into radiative and ohmic channels,

$$\gamma_{\text{rad}}^{(\text{res})} = \beta \gamma_{\text{tot}}^{(\text{res})}, \quad \gamma_{\text{nr}}^{(\text{res})} = (1 - \beta) \gamma_{\text{tot}}^{(\text{res})}, \quad \beta \equiv \frac{\kappa_{\text{rad}}}{\kappa_{\text{rad}} + \kappa_{\text{nr}}} \in (0,1), \quad (7)$$

so the radiative Purcell factor is,

$$F_{\text{rad}} = \beta F_P = \beta \frac{3}{4\pi^2} \left(\frac{\lambda}{n}\right)^3 \frac{Q}{V_{\text{eff}}}. \quad (8)$$

Radiative-rate enhancement grows when (i) the effective volume V_{eff} is small (tight hotspot at the emitter), (ii) the total linewidth κ is moderate (decent quality factor Q), and (iii) the radiative branching ratio β is large, for instance, the bright mode couples predominantly to free-space channels rather than to ohmic loss.

Introducing a narrow discrete resonance (e.g., excitonic/Lorentz pole) with annihilation operator d , frequency ω_0 , and intrinsic width Γ , coupled to the bright QNM with strength J yields to additional Hamiltonian term

$$\frac{H_{\text{narrow}}}{\hbar} = \omega_0 d^\dagger d + (J a^\dagger d + \text{h.c.}). \quad (9)$$

This dressing generates the cavity-like susceptibility

$$\chi_c(\omega) = \frac{1}{\omega - \omega_c + \frac{i\kappa}{2} - \frac{|J|^2}{\omega - \omega_0 + \frac{i\Gamma}{2}}}. \quad (10)$$

i.e., a broad background (bright QNM) interferes with a narrow pathway (discrete pole).

The QOs used here (dielectric nano-inclusions with a narrow Lorentz pole) act as subwavelength permittivity perturbations. To leading order in the contrast $\Delta\epsilon_i(\omega)$ and for volumes $V_i \ll \lambda^3$, the Lippmann-Schwinger (Dyson) equation yields a rank-1 correction to the Toroidal Green tensor [60,61]:

$$\mathbf{G}(\mathbf{r}, \mathbf{r}'; \omega) \cong \mathbf{G}^{(T)}(\mathbf{r}, \mathbf{r}'; \omega) + k_0^2 \sum_i \Delta\epsilon_i V_i \mathbf{G}^{(T)}(\mathbf{r}, \mathbf{r}_i; \omega) \cdot \mathbf{G}^{(T)}(\mathbf{r}_i, \mathbf{r}'; \omega) \quad (11)$$

with $\mathbf{G}^{(T)}$ the toroid-only tensor. Interference between the smooth toroidal LDOS and the narrow inclusion pole produces a Fano line shape in the radiative and nonradiative channels [20,28]:

$$\frac{\gamma_{r,wQO}}{\gamma_0} \propto \frac{(\epsilon+q)^2}{1+\epsilon^2}, \quad \text{with } \epsilon = \frac{\omega - \omega_{QO} - \Delta(\omega)}{\frac{\Gamma_{QO}}{2}}, \quad (12)$$

where q is set by the complex overlap $\mathbf{G}^{(T)}(\mathbf{r}_0, \mathbf{r}_{QO}) \cdot \mathbf{G}^{(T)}(\mathbf{r}_{QO}, \mathbf{r}_0)$ and $\Delta(\omega)$ is the Green-tensor frequency shift (real part of the self-energy). With two detuned inclusions, Eq. (11) adds a cross-term $\mathbf{G}^{(T)} \mathbf{V}_1 \mathbf{G}^{(T)} \mathbf{V}_2 \mathbf{G}^{(T)}$ ($\mathbf{V}_i = k_0^2 \Delta\epsilon_i V_i \mathbf{I}$), yielding two interfering Fano numerators on the same toroidal background and hence a pair of transparency minima. For several detuned QOs Eq. (11) naturally generates cross terms that represent multiple interfering Fano pathways on the same background.

Numerical Methodology

The finite-difference time-domain (FDTD) method is employed to solve Maxwell's curl equations in free space. All simulations are performed using the FDTD solution software package of Ansys-Lumerical which enables 3D simulations of complex electromagnetic interactions between the components of the system. Perfectly Matched Layer (PML) boundary condition is utilized to simulate open-space behaviour. Lorentzian dielectric functions are employed to model QO's electrical response, which is given by

$$\epsilon(\omega) = \epsilon_\infty + \frac{f \omega_0^2}{\omega_0^2 - \omega^2 - i\gamma\omega}$$

where ϵ_∞ is the background permittivity, f is the Lorentzian permittivity and γ is the Lorentzian linewidth. Each QO has a radius of 20 nm, Lorentzian permittivity of 0.2 and Lorentzian linewidth of $\sim 10^{10}$ rad/s. Ag toroid's optical response is implemented from experimental data provided by Johnson & Christy [62], which has major radius R and cross-sectional radius α . QE is modelled as an electric dipole radiating around 850 nm for an aspect ratio of 0.2, and its emission wavelength is adjusted for other configurations to probe their respective resonance

conditions. To ensure numerical accuracy, a fine spatial mesh with element sizes ranging from $\lambda/2600$ to $\lambda/600$ are employed in the near-field region at various QE-TNA separations.

The decay rate in free space is given by,

$$\gamma_0 = \frac{\omega^3 |\mathbf{p}|^2}{3\pi\epsilon_0 \hbar c^3}$$

where, ω is the angular frequency, $|\mathbf{p}|$ is the dipole moment, ϵ_0 is the vacuum permittivity, \hbar is the Planck's constant, and c is the speed of light. To isolate the energy that is emitted as light (radiated power) in the presence of QE-TNA system, far-field power monitors are used. The radiative decay rate is then [43]

$$\gamma_{rad} = \frac{P_{rad}}{P_0} \gamma_0$$

where P_{rad} is the power captured by monitors in the far-field. Total decay rate is then,

$$\gamma_{tot} = \frac{P_{tot}}{P_0} \gamma_0$$

where P_{tot} is the power calculated by monitors that are located in the near field. Straightforwardly, the non-radiative decay rate can be calculated as

$$\gamma_{nonrad} = \gamma_{tot} - \gamma_{rad}.$$

Near-field power monitors are placed to encompass the emitting dipole and TNA-QO hybrid system, allowing for the collections of all energy flows, including those altered by the antenna's near-field coupling, which is

$$P_{tot} = \oint_s \mathbf{S} \cdot d\mathbf{A}$$

where \mathbf{S} is the Poynting vector. Similarly,

$$P_{rad} = \oint_{S_{far}} \mathbf{S} \cdot d\mathbf{A}$$

is the power computed using far-field monitors in the simulation domain, excluding non-radiative losses and isolating the radiative decay accelerated by localised surface plasmon resonance (LSPR).

The emitter-antenna (QE-TNA) distance dependence of the QE is fitted by application of exponential curve in the form:

$$y_i(x) = \exp(a + bx + cx^2)$$

where the constant coefficients a , b , and c are obtained as $a = 8.40839$, $b = -0.16056$, $c = 0.00162$, for radiative decay, and $a = 7.52683$, $b = -0.20485$, $c = 0.00243$ for the non-radiative decay rate.

Acknowledgments

E.O.P acknowledges the support from TUBITAK (222N308, CHIST-ERA) and BILKENT University- TUBITAK BILGEM Consultancy Call for Research (BIL2).

Author Contributions

A.G ran the simulations, performed the calculations, extracted the the raw data forming the basis of the shown results and contributed to the formation of the manuscript. E.O.P conceptualized and supervised the idea and majorly contributed to the formation of the manuscript by creation of final figures and the main text.

Competing interests

The authors declare no competing interests.

Data availability

All data necessary to evaluate the results presented in this work are included within the paper. Additional datasets supporting the findings of this study are available from the corresponding author upon reasonable request.

References

- [1] Y. Wy, H. Jung, J. W. Hong, and S. W. Han, Exploiting Plasmonic Hot Spots in Au-Based Nanostructures for Sensing and Photocatalysis, *Acc. Chem. Res.* **55**, 831 (2022).
- [2] S. A. Maier, M. L. Brongersma, P. G. Kik, S. Meltzer, A. A. G. Requicha, and H. A. Atwater, Plasmonics—A Route to Nanoscale Optical Devices, *Adv. Mater* **13**, 1501 (2001).
- [3] S. A. Maier and others, *Plasmonics: Fundamentals and Applications*, Vol. 1 (Springer, 2007).
- [4] K. Kneipp, Y. Wang, H. Kneipp, L. T. Perelman, I. Itzkan, R. R. Dasari, and M. S. Feld, Single Molecule Detection Using Surface-Enhanced Raman Scattering (SERS), *Phys. Rev. Lett.* **78**, 1667 (1997).
- [5] E. Ozbay, Plasmonics: Merging photonics and electronics at nanoscale dimensions, *Science* (1979) **311**, 189 (2006).
- [6] A. Gulucu and E. O. Polat, Optically Switchable Fluorescence Enhancement at Critical Interparticle Distances, *Adv. Theory Simul.* **8**, e01134 (2025).
- [7] R. Sharma, N. K. Pathak, and R. P. Sharma, Computational Study of Plasmon Interaction in Organic Media: a Comparison Between Analytical and Numerical Model for Dimer, *Plasmonics* **13**, 1775 (2018).
- [8] Y. F. Xiao, Y. C. Liu, B. B. Li, Y. L. Chen, Y. Li, and Q. Gong, Strongly enhanced light-matter interaction in a hybrid photonic-plasmonic resonator, *Phys. Rev. A* **85**, 031805 (2012).
- [9] J. Cao, T. Sun, and K. T. V. Grattan, Gold nanorod-based localized surface plasmon resonance biosensors: A review, *Sens. Actuators. B: Chem.* **195**, 332 (2014).
- [10] T. Kaelberer, V. A. Fedotov, N. Papasimakis, D. P. Tsai, and N. I. Zheludev, Toroidal Dipolar Response in a Metamaterial, *Science* (1979) **330**, 1510 (2010).
- [11] N. Papasimakis, V. A. Fedotov, V. Savinov, T. A. Raybould, and N. I. Zheludev, Electromagnetic toroidal excitations in matter and free space, *Nat. Mater* **15**, 263 (2016).

- [12] A. Mary, A. Dereux, and T. L. Ferrell, Localized surface plasmons on a torus in the nonretarded approximation, *Phys. Rev. B Condens. Matter Mater. Phys.* **72**, 155426 (2005).
- [13] T. Warnakula, S. D. Gunapala, M. I. Stockman, and M. Premaratne, Broken poloidal symmetry and plasmonic eigenmodes on a torus, *Phys. Rev. B* **101**, 115426 (2020).
- [14] T. V. Teperik and A. Degiron, Numerical analysis of an optical toroidal antenna coupled to a dipolar emitter, *Phys. Rev. B Condens. Matter Mater. Phys.* **83**, 245408 (2011).
- [15] C. M. Dutta, T. A. Ali, D. W. Brandl, T. H. Park, and P. Nordlander, Plasmonic properties of a metallic torus, *J. Chem. Phys.* **129**, (2008).
- [16] J. Aizpurua, P. Hanarp, D. S. Sutherland, M. Käll, G. W. Bryant, and F. J. García de Abajo, Optical Properties of Gold Nanorings, *Phys. Rev. Lett.* **90**, 4 (2003).
- [17] H. E. M. Purcell, *Spontaneous Emission Probabilities at Radio Frequencies*, in *Confined Electrons and Photons: New Physics and Applications* (Springer, 1995).
- [18] K. V. Garapati, M. Salhi, S. Kouchekian, G. Siopsis, and A. Passian, Poloidal and toroidal plasmons and fields of multilayer nanorings, *Phys. Rev. B* **95**, 165422 (2017).
- [19] M. F. Limonov, M. V. Rybin, A. N. Poddubny, and Y. S. Kivshar, Fano resonances in photonics, *Nat. Photonics* **11**, 543 (2017).
- [20] U. Fano, Effects of Configuration Interaction on Intensities and Phase Shifts, *Phys. Rev.* **124**, 1866 (1961).
- [21] M. Pelton, S. D. Storm, and H. Leng, Strong coupling of emitters to single plasmonic nanoparticles: exciton-induced transparency and Rabi splitting, *Nanoscale* **11**, 14540 (2019).
- [22] N. Liu, L. Langguth, T. Weiss, J. Kästel, M. Fleischhauer, T. Pfau, and H. Giessen, Plasmonic analogue of electromagnetically induced transparency at the Drude damping limit, *Nat. Mater* **8**, 758 (2009).
- [23] H. Leng, B. Szychowski, M. C. Daniel, and M. Pelton, Strong coupling and induced transparency at room temperature with single quantum dots and gap plasmons, *Nat. Commun.* **9**, 1 (2018).
- [24] M. Pelton, S. K. Gray, and X. Wu, Quantum-dot-induced transparency in a nanoscale plasmonic resonator, *Opt. Express* **18**, 23633 (2010).
- [25] S. Zhang, D. A. Genov, Y. Wang, M. Liu, and X. Zhang, Plasmon-induced transparency in metamaterials, *Phys. Rev. Lett.* **101**, 047401 (2008).
- [26] Y. Zheng et al., Fano Resonance in Single-Molecule Junctions, *Angew. Chem. - Int. Ed.* **61**, 10097 (2022).
- [27] A. E. Miroshnichenko, S. Flach, and Y. S. Kivshar, Fano resonances in nanoscale structures, *Rev. Mod. Phys.* **82**, 2257 (2010).
- [28] B. Luk'Yanchuk, N. I. Zheludev, S. A. Maier, N. J. Halas, P. Nordlander, H. Giessen, and C. T. Chong, The Fano resonance in plasmonic nanostructures and metamaterials, *Nat. Mater* **9**, 707 (2010).

- [29] M. Pelton, S. K. Gray, and X. Wu, Quantum-dot-induced transparency in a nanoscale plasmonic resonator, *Opt. Express* **18**, 23633 (2010).
- [30] H. Leng, B. Szychowski, M. C. Daniel, and M. Pelton, Strong coupling and induced transparency at room temperature with single quantum dots and gap plasmons, *Nat. Commun.* **9**, 4012 (2018).
- [31] J. Yan, C. Ma, P. Liu, C. Wang, and G. Yang, Generating scattering dark states through the Fano interference between excitons and an individual silicon nanogroove, *Light Sci. Appl.* **6**, e16197 (2016).
- [32] R. A. Shah, N. F. Scherer, M. Pelton, and S. K. Gray, Ultrafast reversal of a Fano resonance in a plasmon-exciton system, *Phys. Rev. B* **88**, 075411 (2013).
- [33] A. Hassanfiroozi, P. S. Huang, S. H. Huang, K. I. Lin, Y. T. Lin, C. F. Chien, Y. Shi, W. J. Lee, and P. C. Wu, A Toroidal-Fano-Resonant Metasurface with Optimal Cross-Polarization Efficiency and Switchable Nonlinearity in the Near-Infrared, *Adv. Opt. Mater* **9**, 2101007 (2021).
- [34] Q. Mi, T. Sang, Y. Pei, C. Yang, S. Li, Y. Wang, and B. Ma, High-quality-factor dual-band Fano resonances induced by dual bound states in the continuum using a planar nanohole slab, *Nanoscale Res. Lett.* **16**, 150 (2021).
- [35] N. Papasimakis, V. A. Fedotov, N. I. Zheludev, and S. L. Prosvirnin, Metamaterial Analog of Electromagnetically Induced Transparency, *Phys. Rev. Lett.* **101**, 253903 (2008).
- [36] S. Zhang, D. A. Genov, Y. Wang, M. Liu, and X. Zhang, Plasmon-Induced Transparency in Metamaterials, *Phys. Rev. Lett.* **101**, 047401 (2008).
- [37] E. O. Polat, Z. Artvin, Y. Şaki, A. Bek, and R. Sahin, Continuous and Reversible Electrical Tuning of Fluorescent Decay Rate via Fano Resonance, *ArXiv Preprint* 2412.20199 (2024).
- [38] D. A. B. Miller, D. S. Chemla, T. C. Damen, A. C. Gossard, W. Wiegmann, T. H. Wood, and C. A. Burrus, Band-Edge Electroabsorption in Quantum Well Structures: The Quantum-Confined Stark Effect, *Phys. Rev. Lett.* **53**, 2173 (1984).
- [39] Y. Miao, R. C. Boutelle, A. Blake, V. Chandrasekaran, C. J. Sheehan, J. Hollingsworth, D. Neuhauser, and S. Weiss, Super-resolution Imaging of Plasmonic Near-Fields: Overcoming Emitter Mislocalizations, *J. Phys. Chem. Lett.* **13**, 4520 (2022).
- [40] C. Lee, B. Lawrie, R. Pooser, K. G. Lee, C. Rockstuhl, and M. Tame, Quantum Plasmonic Sensors, *Chem. Rev.* **121**, 4743 (2021).
- [41] W. Bogaerts, D. Pérez, J. Capmany, D. A. B. Miller, J. Poon, D. Englund, F. Morichetti, and A. Melloni, Programmable photonic circuits, *Nature* **586**, 207 (2020).
- [42] X. Duan, S. Kamin, and N. Liu, Dynamic plasmonic colour display, *Nat. Commun.* **8**, 1 (2017).
- [43] L. Novotny and B. Hecht, *Principles of Nano-Optics* (Cambridge University Press, 2012).
- [44] R. Carminati, J. J. Greffet, C. Henkel, and J. M. Vigoureux, Radiative and non-radiative decay of a single molecule close to a metallic nanoparticle, *Opt. Commun.* **261**, 368 (2006).

- [45] G. W. Wen, J. Y. Lin, H. X. Jiang, and Z. Chen, Quantum-confined Stark effects in semiconductor quantum dots, *Phys. Rev. B* **52**, 5913 (1995).
- [46] I. Niehues, E. D. S. Nysten, R. Schmidt, M. Weiß, and D. Wigger, Excitons in quantum technologies: The role of strain engineering, *MRS Bull.* **49**, 958 (2024).
- [47] H. Bahmani Jalali, L. De Trizio, L. Manna, and F. Di Stasio, Indium arsenide quantum dots: an alternative to lead-based infrared emitting nanomaterials, *Chem. Soc. Rev.* **51**, 9861 (2022).
- [48] S. Castelletto, F. A. Inam, S. I. Sato, and A. Boretti, Hexagonal boron nitride: a review of the emerging material platform for single-photon sources and the spin–photon interface, *Beilstein J. Nanotechnol.* **11**, 740 (2020).
- [49] D. Liu, F. Kaiser, V. Bushmakina, E. Hesselmeier, T. Steidl, T. Ohshima, N. T. Son, J. Ul-Hassan, Ö. O. Soykal, and J. Wrachtrup, The silicon vacancy centers in SiC: determination of intrinsic spin dynamics for integrated quantum photonics, *Npj Quantum Inf.* **10**, 72 (2024).
- [50] M. Liu et al., Multifunctional metasurfaces enabled by simultaneous and independent control of phase and amplitude for orthogonal polarization states, *Light Sci. Appl.* **10**, 1 (2021).
- [51] T. Roesel, A. Dahlin, M. Piliarik, L. W. Fitzpatrick, and B. Špačková, Label-free single-molecule optical detection, *Npj Biosensing* 2025 2:1 **2**, 1 (2025).
- [52] S. W. Chong, Y. Shen, S. Palomba, and D. Vigolo, Nanofluidic Lab-On-A-Chip Systems for Biosensing in Healthcare, *Small* **21**, 2407478 (2025).
- [53] N. A. Salama, S. M. Alexere, S. S. A. Obayya, and M. A. Swillam, Silicon-based double fano resonances photonic integrated gas sensor, *Sci. Rep.* **14**, (2024).
- [54] H. J. Chen, Multiple-Fano-resonance-induced fast and slow light in the hybrid nanomechanical-resonator system, *Phys. Rev. A* **104**, 013708 (2021).
- [55] Y. Huo, T. Jia, T. Ning, C. Tan, S. Jiang, C. Yang, Y. Jiao, and B. Man, A low lasing threshold and widely tunable spaser based on two dark surface plasmons, *Sci. Rep.* **7**, 1 (2017).
- [56] N. K. Emani, T. F. Chung, A. V. Kildishev, V. M. Shalae, Y. P. Chen, and A. Boltasseva, Electrical modulation of fano resonance in plasmonic nanostructures using graphene, *Nano Lett.* **14**, 78 (2014).
- [57] C. Sauvan, J. P. Hugonin, I. S. Maksymov, and P. Lalanne, Theory of the Spontaneous Optical Emission of Nanosize Photonic and Plasmon Resonators, *Phys. Rev. Lett.* **110**, 237401 (2013).
- [58] P. T. Kristensen, R. C. Ge, and S. Hughes, Normalization of quasinormal modes in leaky optical cavities and plasmonic resonators, *Phys. Rev. A* **92**, 053810 (2015).
- [59] E. A. Muljarov and W. Langbein, Exact mode volume and Purcell factor of open optical systems, *Phys. Rev. B* **94**, 235438 (2016).
- [60] W. Cho. Chew, *Waves and fields in inhomogeneous media* (John Wiley & Sons, 1999).
- [61] O. J. F. Martin, C. Girard, and A. Dereux, Generalized Field Propagator for Electromagnetic Scattering and Light Confinement, *Phys. Rev. Lett.* **74**, 526 (1995).

- [62] P. B. Johnson and R. W. Christy, Optical Constants of the Noble Metals, Phys. Rev. B **6**, 4370 (1972).